Tungsten Carbide: A Versatile Additive to Get Trace Alkaline-earth Oxide Impurities out of ZrB2 based Ceramics

Zou, Ji; D'Angio', Andrea; Ma, Haibin; Zhang, Guojun

DOI:
10.1016/j.scriptamat.2017.12.033

Document Version
Peer reviewed version

Citation for published version (Harvard):
Zou, J, D'Angio', A, Ma, H & Zhang, G 2018, 'Tungsten Carbide: A Versatile Additive to Get Trace Alkaline-earth Oxide Impurities out of ZrB2 based Ceramics', *Scripta Materialia*, vol. 147, pp. 40-44.
https://doi.org/10.1016/j.scriptamat.2017.12.033

Tungsten Carbide: A Versatile Additive to Get Trace Alkaline-earth Oxide Impurities out of ZrB_2 based Ceramics

Ji Zou[a*], Hai-Bin Ma[b*], Andrea D'Angio'[a] and Guo-Jun Zhang[b*]

[a] School of Metallurgy and Materials, University of Birmingham, B15 2TT, UK
[b] State Key Laboratory for Modification of Chemical Fibers and Polymer Materials, Research Institute of Functional Materials, Donghua University, Shanghai, 201620, China

* Corresponding author, e-mail: zouji1983@gmail.com; mahaibin0914@sina.com; gjzhang@dhu.edu.cn.

Abstract

In this work, trace amounts of alkaline-earth oxide impurities (M_xO_y), M=Mg, Ca and Al, are identified from different graded ZrB_2 based ceramics. The reactions in M_xO_y-WC systems at high temperature are therefore investigated via X-Ray diffraction and element analysis, which have been further supported by thermodynamic calculations. Since M_xO_y with low melting point deteriorates the high temperature performance of ceramics, the effective role of WC on strong ZrB_2-SiC-WC ceramics is re-considered: apart from the contribution on removing of ZrO_2, WC serves as a versatile additive with capacity to remove different oxide impurities from the ceramic body.

Keywords
Borides; alkaline earth; ceramics; surface oxygen impurities;

Strong ceramics are generally desired for their service at high temperature [1-3]. On the one hand, for a ceramic part with a fixed geometry, a higher strength value means that it could bear a greater load before fracture; on the other hand, thermal shock resistance of ceramics with a higher strength will be substantially improved, since the thermal shock parameters (R' and R'') for crack initiation are proportional to the

strength level with other things being equal [4]. According to the theory of Griffith's fracture, at room temperature, the strength of brittle ceramics is governed by the dimension of its largest defects, in terms of void, inclusion and crack et al. However, these effects become less important with increasing the temperature, due to the fact that some of the cracks, especially for the machine-generated ones, could be healed during the high-temperature testing [5, 6]. Therefore, in absence of low melting phases at the grains junctions, the strength of ceramics at higher temperature relies predominantly on their intrinsic property: bonding characters, lattice structures, etc. Previous research in ZrB_2-SiC ceramics shows that the effect of impurity phases plays a decisive role [6].

The impurities could be originated from the raw powders, collected during the various steps during ceramic processing, or contaminated in the environment for sintering. The softening of these impurities at high temperature is an indicator for the strength degradation of ceramics. In fact, adjusting the chemistry of the impurities have been demonstrated to be an effective route to obtain SiC [7-8] and Si_3N_4 ceramics [9-10] with better high temperature performance. Alternatively, these impurities could be removed by selecting suitable additives to achieve a cleaner grain boundary. Ceramics with tightened grain boundary have exhibited superior strength [7, 11-13]. Boride ceramics are a class of important engineering ceramics and benchmark materials liable to be affected by the oxide impurities. For instance, in ZrB_2 ceramics, oxide impurities are present on the surface oxide layer of the ZrB_2 powders, which are assumed to be amorphous B_2O_3 and crystalline ZrO_2 [14-15]. B_2O_3 could be eliminated from the ceramic body by its evaporation in vacuum, whereas ZrO_2 has to be removed chemically by its reaction with WC or other carbides through Reaction 1 [16].

$$ZrO_2+3WC= ZrC + 3W + 2CO\ (g) \qquad \text{Reaction 1}$$

Benefiting from the WC additions, strong ZrB_2-SiC-WC ceramics with clean grain

boundary and without any strength degradation up to 2000°C have been successfully developed [11-12]. However, observations on the boride ceramics have suggested that besides B_2O_3 and ZrO_2, other oxides with low melting temperature, e.g. alkaline-earth oxide, have been detected in the as sintered ZrB_2 body from different research groups *cf.* Table I. The coexistence of various oxides in ZrB_2 based ceramics implies that the mechanism for the impurity removal in ZrB_2 by WC additions (Reaction 1) is still unclear. In addition, alkaline-earth oxides have been commonly observed from the ceramic product [17] and their influence is mostly negative [18]: deterioration of the corrosion resistance to molten metals and high temperature strength are amongst the major detrimental effects. On this basis, the aim of the study is to understand the role of WC on removing the impurities in boride ceramics, to provide new insights on understanding the mechanism for strong ZrB_2-SiC-WC ceramics at higher temperatures and to seek a practical way to eliminate the alkaline-earth oxides from the ceramic body.

In order to identify the oxide impurities in ZrB_2 based ceramics properly, ZrB_2-SiC [5] and ZrB_2-ZrC ceramics [19] prepared from different ZrB_2 suppliers were chosen for a further characterization. The oxide impurities observed in ZrB_2 based ceramics have been summarized and listed in Table I. The impurities in the starting powders and sintered ceramics were mainly examined by a transmission electron microscope equipped with energy dispersive X-ray spectroscopy (EDS). Since impurities such as CaO, MgO and Al_2O_3 were identified from the EDS analysis,, three powder mixtures, namely, CaO-WC, MgO-WC and Al_2O_3-WC, were prepared by mixing the corresponding oxide (M_xO_y, M refers to Al, Mg and Ca, similarly hereinafter) with WC powder (Hard alloy Co. Ltd, Zhuzhou, China, particle size <1μm) based on a molar ratio of 1:5. Although the amount of MgO in the impurity (Fig.1d, 1h and S1b) is limited, MgO-WC system was investigated since MgO is the major impurity in the boride powder synthesized by magnesiothermic reduction [20]. A larger proportion of WC was intentionally chosen in the composition because excess WC had been added

in ZrB_2-SiC matrix compared with corresponding oxygen levels. For example, 3-5vol%WC (4.0-6.6mol%) was always added in to ZrB_2 powders with a documented oxygen level of <1wt% (ZrO_2 content<0.58mol%) [11-12]. 3Y-ZrO_2 balls and ethanol were used as the media and the solvent for the mixing. As mixed slurry were dried through rotary evaporation and then crashed and meshed into fine powders. The pellets with diameter of 10mm were obtained by uniaxial dry pressing the powders at ~100MPa for 30s, which were followed by heating them up at 10°C/min to 1600°C in a graphite furnace. The entire heat treatment also includes an isothermal step at 1600°C for 0.5h and the vacuum level in the furnace during holding was maintained at ~5Pa.

After removing the surface layers, the phase assemblage of as-mixed and 1600°C treated samples was firstly determined by X-ray diffraction (XRD). The composition of the samples before and after heat treatment was also analyzed by X-ray fluorescence (XRF) analysis. Finally, Glow Discharge Mass Spectrometry (GDMS) was employed to compare some impurity changes for the hot-pressed ZrB_2-SiC ceramics with and without 5vol%WC doping.

Independently from the implementation of boro/carbothermal reduction routes, impurities could be clearly detected from the as-synthesized powder (Fig.1a, b and e, f). These phases were easily recognized as they are characterized by low contrast due to their high content of light elements and are generally located separately from the ZrB_2 agglomerates. Similarly, amorphous phase based on Zr-Si-K-Ca-Mg-Cl-O (corresponding electron diffraction pattern and EDS spectrum are shown in Fig.S1) is detectable from commercial available ZrB_2 powder (H.C. Starck, Grade B), *cf.* Fig.1i and 1j. After sintering, amorphous phase appears in the form of impurities as shown in Fig 1c and 1g, which generally exist in the triple junction of the grain boundaries and adjacent to one or more SiC grains, *cf.* Fig.1c and g. Although their composition varied marginally for different samples and at different locations within the single sample, they generally included Al, Mg, Ca, O, Y and occasionally contained carbon

and silicon, Fig.1d and 1h. These impurities are not necessarily associated with the SiC phases in the as-sintered ceramics and easy to be found (Fig.1k and 1l). For example, crystallized ZrO_2 covered by amorphous phase with Al-Mg-Ca-Si-O were disclosed by the elemental mappings (Fig.1m) from dense ZrB_2-ZrC ceramics. Based on a summary in Table I and the above microstructure characterization, it seems that the existence of these impurities in ZrB_2 ceramics is inevitable, regardless of the powder source, the composition of the ceramics and even the research group who handles the process to produce the ceramics.

Since these alkaline-earth oxides have not been detected in ZrB_2-SiC sample with WC additions [13], their possible removals by WC is thus probable. The reactions in M_xO_y -WC systems were investigated accordingly to address the issue. Although the peak intensity of MgO and CaO is relatively weak, both of them still could be indexed from the starting powder mixtures (Fig.2a). After a heat treatment at 1600°C, nevertheless, the diffraction peaks of MgO and CaO disappeared while a series of peaks belong to W_2C were found, together with the unconsumed WC. With regards to Al_2O_3-WC sample, no visible Al_2O_3 peaks could be seen either from the starting powder or the pellet after heat treatment (Fig.2a and b). Typical peak broadening was found in a separate XRD pattern collected from the starting Al_2O_3 powder only (Fig.S2), indicating a finer grain size and reduced crystallinity, which can well explain its absence from the XRD pattern (Fig.2a). Further indexing of the pattern suggests the Al_2O_3 powder has a cubic symmetry of the γ polytype. The absence of Al_2O_3 peaks after heat treatment suggests Al_2O_3 might have reacted with WC, if not, α-Al_2O_3 peaks would have been visible in Fig.2b. The phase transformation from γ-Al_2O_3 to α-Al_2O_3 with improved crystallinity normally takes place at ~650°C and completes below 1000°C, which has been well documented in the literature [21].

In order to verify some hypotheses from the XRD analysis, the composition of the pellets before and after the heat treatment has been determined quantitatively by XRF and the results were compared through the histogram in Fig.3. Clearly, significant decrease in the concentration of MgO, CaO and Al_2O_3 has been found after heat

treatment. In fact, no noticeable amount of CaO and MgO had been analyzed from the treated pellets. Combing these observations with the XRD results, the following reaction mechanisms might take place during the heat treatment at 1600 °C and the loss of Ca, Mg and Al in vapour phase caused their reduction in Fig.3.

$$CaO + 2WC = W_2C + CO + Ca\ (g) \qquad \text{Reaction 2}$$

$$MgO + 2WC = W_2C + CO + Mg\ (g) \qquad \text{Reaction 3}$$

$$Al_2O_3 + 6WC = 3W_2C + 3CO + 2Al\ (g) \qquad \text{Reaction 4}$$

For MgO-WC system, 2 mol of WC are sufficient to reduce 1mol of MgO in to Mg (g), CO(g) and W_2C. Considering the molar ratio between WC and MgO in the powder mixture was set as 5:1, excess WC is expected after the reaction which fits well with the XRD analysis (Fig.2b). Similar considerations apply for the CaO-WC system. In Al_2O_3-WC system, however, 6 mol of WC are required to react with 1 mole of Al_2O_3 according to Reaction 4. Consequently, some WC must be further oxidized into W to consume the extra Al_2O_3 and balance the equation (Reaction 5). Coincidently, a series of W peaks were found in the Al_2O_3–WC pellet after heat treatment (Fig.2b), while they were not observed from MgO (CaO)-WC pellets. This further supports the proposed reaction path shown above.

$$Al_2O_3 + 3WC = 3W + 3CO + 2Al\ (g) \qquad \text{Reaction 5}$$

According to the XRF results in Fig.3, various oxide impurities were present in the starting MgO, CaO and Al_2O_3 powders. Interestingly, with the reduction of M_xO_y by WC, the levels of these impurities also decreased. For instance, measured SiO_2, Cr_2O_3, Al_2O_3 and Fe_2O_3 content in the starting MgO powder is 0.246, 0.447, 0.049 and 0.125 wt%, respectively, these values decreased to <0.001, <0.001, 0.03 and 0.07 wt% after the heat treatment. Likewise, 0.675wt% Na_2O, 0.044wt% Al_2O_3, 0.226wt% SiO_2 and 0.442wt% Cr_2O_3 are present in raw CaO powder, these numbers changed to <0.001,

0.087, 0.069 and 0.197 wt%. To summarize, WC also shows the potentials to reduce the amount of other oxide impurities, apart from M_xO_y, from the ceramic body, e.g. Cr_2O_3, SiO_2 etc.

The detailed processes for removing M_xO_y by WC could be illustrated via thermodynamic calculations as displayed in Fig.4. Consistently with the experiments, M_xO_y are unstable when WC is present and they are heated at high temperature in a mild vacuum level (5Pa in this case). For MgO-WC and CaO-WC systems (4a and 4b), a significant drop of the oxide amount occurs at ~1000°C and ~1200°C, respectively. Meanwhile, gaseous reaction products, such as Mg(g), Ca(g) and CO(g), start to be released above that temperature. The vapours of magnesium and calcium reach their maximum at ~1250 °C and ~1350 °C, calculations also predict that W_2C is the only solid product from that temperature to 2000°C in both systems. The reactions in Al_2O_3-WC system are more complicated, but clearly, Al_2O_3 starts to react with WC at ~1200°C. The formation of W_2C indicates that Reaction 4 becomes favorable above ~1100°C, which is prior to Reaction 5, because the occurrence of W is found to be at ~1400°C. Although AlO_2 is predicted to be a stable phase in Al_2O_3-WC system between 1300 and 1700°C (Fig.4c), its existence has not been observed in this work. It should be noted that the reduction of these oxides is strongly related to the WC additions. When WC is absent, the decomposition of MgO and CaO requires a temperature over 1800°C (Fig.3d and 3e) while no remarkable degradation was calculated in Al_2O_3 up to 2000°C under the same vacuum level. Incorporating WC in to the oxide system leads to the formation of CO as a gaseous byproduct. The continuous evacuation of CO (g) and M (g) out of the furnace chamber is helpful to reduce the temperature at which Reactions (2)-(5) become favorable by decreasing the Gibbs energy change of each reaction. Put the results from Fig.3 and Fig.4 together, it has demonstrated that WC serves as a versatile additive, showing ability to get different alkaline/alkaline-earth oxide impurities eliminated from the ceramic body at a moderate processing conditions, e.g. temperature <1600°C and a mild vacuum level of ~5Pa.

Since yttria and iron oxide used to be detected from ZrB_2-SiC ceramics by TEM-EDS (Fig.1h and Table I), their possible reductions by the reaction with WC are also considered here. As displayed in Fig.S3, although the removal of Y_2O_3 and Fe_2O_3 by WC is adequately possible, fully removal of Y_2O_3 require higher temperatures (>1800°C). More importantly, significant amount of Y(g) and Fe(g) vapors can only be generated above 1750°C and 1600°C, while the densification of ceramics had already started at that temperature. Taking into account that (1) Y and Fe atoms could be incorporated in to ZrB_2 lattice below that temperature and form solid solution with ZrB_2, (2) the escaping gaseous Y(g) and Fe(g) from denser ceramics is extremely difficult, this implies that the complete removal of these impurities from ZrB_2 body by WC becomes hard to achieve. The Y content obtained by GDMS in hot pressed ZrB_2-SiC (ZS) and ZrB_2-SiC-WC (ZSW) ceramics (Table I) is 0.86 and 0.76 wt %, showing a good consistency with the proposed.

Zhang's work revealed that ZrO_2 impurity in ZrB_2 could be removed by reaction with WC or B_4C, the elimination of oxide impurities has been proved to play a key role on enhancing the pressureless densification of ZrB_2 ceramics [16]. However, compared with WC, the removal of M_xO_y by B_4C is incomplete. Calculations (Fig.S4) show that in CaO-B_4C system, the evaporation of Ca (g) is retarded by the formation of two solids: CaB_6 and $Ca_3B_2O_6$. Remarkable amount of gaseous substance is only observed when the T > 1600°C. At equilibrium, 75% of input Ca still remains in the CaO-B_4C system even at an extreme condition (2000°C, 5Pa). The flexural strength of ZrB_2-SiC-B_4C ceramics degraded gradually starting from 1300°C while ZrB_2-SiC-WC ceramics exhibit even higher strength value at 1600°C compared to that at room temperature [11, 23] *c.f.* Table I. Considering the softening of oxide impurities above their glass transition temperature have been proposed to be responsible for the strength drop of ZrB_2-SiC ceramics with a temperature increase [5], the improved high temperature performance in ZSW might be attribute to the synergetic oxide impurities removal effect resulted from the addition of WC.

In this work, trace amounts of alkaline-earth oxide impurities, M_xO_y (M=Mg, Ca and Al) were identified from various as-sintered ZrB_2 based UHTCs. The removal of M_xO_y in ZrB_2 based UHTCs by WC additions has been proved. Thermodynamic calculations indicated that M_xO_y could be fully reduced in to Mg, Ca or Al by suitable amounts of WC under mild temperature and vacuum level, further elimination of these metal species from the ceramic body could be realized through their evaporation, hence, "clean" ZrB_2 based ceramics free of low melting point oxides could be obtained. The current finding provides a reasonable explanation for understanding the excellent behavior of ZrB_2-SiC-WC ceramics at high temperature.

Acknowledgements

Financial supports from the National Natural Science Foundation of China (No. 51532009 and 51272266) and NSFC-JSPS cooperation program (No. 51611140121).

Reference

[1] Y. Waku, N. Nakagawa, T. Wakamoto, H. Ohtsubo, K. Shimizu and Y. Kohtoku, Nature 389(1997) 49-52.

[2] N.P. Padture, Nat. Mater. 15 (2016) 804-09.

[3] W.G. Fahrenholtz, G.E. Hilmas, Scr. Mater. 129 (2017) 94-99.

[4] Andrew A. Buchheit, Greg E. Hilmas, William G. Fahrenholtz and Douglas M. Deason, J. Am. Ceram. Soc. 92 (2009) 1358-1361.

[5] Ji Zou, Guo-Jun Zhang, Chun-Feng Hu, Toshiyuki Nishimura, Yoshio Sakka, Hidehiko Tanaka, Jef Vleugels, Omer Van der Biest, J. Eur. Ceram. Soc. 32 (2012) 2519-2527.

[6] Ji Zou, Guo-Jun Zhang, Jef Vleugels, Omer Van der Biest, J. Eur. Ceram. Soc. 33 (2013) 1609-1614.

[7] Young-Wook Kim, Seung Hoon Jang, Toshiyuki Nishimura, Si-Young Choi and Sung-Dae Kim, J. Eur. Ceram. Soc. 37 (2017) 4449-4455.

[8] Y.W. Kim, Y.S. Chun, T. Nishimura, M. Mitomo, Y.H. Lee, Acta Mater. 55 (2007) 727-736.

[9] H.Klemm, M.Herrmann, T.Reich and W.Hermel, J. Eur. Ceram. Soc. 7 (1991) 315-318.

[10] Shuqi Guo, Naoto Hirosaki, Yoshinobu Yamamoto, Toshiyuki Nishimura and Mamoru Mitomo, Scr. Mater. 45(2001) 867-874.

[11] Ji Zou, Guo-Jun Zhang, Chun-Feng Hu, Toshiyuki Nishimura, Yoshio Sakka, Jef Vleugels, Omer Van Der Biest, J. Am. Ceram. Soc. 95(2012) 874-878.

[12] Laura Silvestroni, Hans-Joachim Kleebe, William G. Fahrenholtz and Jeremy Watts, Sci. Rep. 7(2017) 40730.

[13] Hai-Bin Ma, Ji Zou, Jing-Ting Zhu, Ping Lu, Fang-Fang Xu, Guo-Jun Zhang, Acta Mater. 129(2017) 159-169.

[14] W. G. Fahrenholtz, G. E. Hilmas, S. C. Zhang, S. Zhu, J. Am. Ceram. Soc. 91 (2008) 1398-1404.

[15] Hai-Bin Ma, Ji Zou, Ping Lu, Jing-Ting Zhu, Zheng-Qian Fu, Fang-Fang Xu, Guo-Jun Zhang, Scr. Mater. 127 (2017) 160-164.

[16] S. C. Zhang, G. E. Hilmas, W. G. Fahrenholtz, J. Am. Ceram. Soc. 89 (2006) 1544-1550.

[17] Charo Martínez-Lebrusant and Flora Barba, Analyst, 115(1990) 1335-1338.

[18] M. Oliveira, S. Agathopoulos and J. M. F. Ferreira, J. Mater. Res.17 (2012) 641-674.

[19] A D'Angio, J Zou, J Binner, Hai-Bin Ma, GE Hilmas, WG Fahrenholtz, J. Eur. Ceram. Soc. 38 (2018) 391-402.

[20] Wang Weimin, Fu Zhengyi, Wang Hao and Yuan Runzhang, J. Mater. Process. Technol. 128(2002) 162-168.

[21] Balaraman Sathyaseelan, Iruson Baskaran and Kandasamy Sivakumar, Soft Nanoscience Letters, 3(2013) 69-74.

[22] D. Pham, J.H. Dycus, J.M. LeBeau, M Venkateswara, K. Mulidharan, and E.L. Corral, J. Am. Ceram. Soc. 99(2016) 2585-92.

[23] Eric W. Neuman, Gregory E. Hilmas and William G. Fahrenholtz, J. Eur. Ceram. Soc. 35(2015) 463-476.

Table and Figure captions

Table caption:

Table I Typical oxide impurities observed in ZrB_2 based ceramics from different research groups, including their processing details and the corresponding flexural strength at room temperature (RT) and 1600^{o}C.

Figure Caption:

Fig. 1 Typical oxide impurities in ZrB_2 powders and corresponding ceramics observed by TEM: (a) (b) ZrB_2 powders with different magnifications synthesized from ZrO_2 and B_4C, (e) (f) ZrB_2 powders synthesized from ZrO_2, B_4C and C, (i)(j) commercial ZrB_2 powder without any treatment from H.C. Starck (Grade B). Arrowed in 1c and 1g are the oxide impurities in the sintered ZrB_2-SiC ceramics using powders from 1a and 1e, corresponding EDS spectra on the impurities phase highlighted in 1c and 1g are shown in 1d and 1h, respectively. The polished surface of ZrB_2-10vol%ZrC ceramics is shown in Fig. 1k with corresponding Al mapping (Fig.1l). The morphology and elemental mappings of an oxide inclusion in ZrB_2-ZrC ceramics are displayed in Fig. 1m. Processing details of these ceramics refer to reference [4, 18].

Fig.2 XRD patterns of (a) as-mixed and (b) as-treated M_xO_y-WC pellets, the treatment was performed at 1600^{o}C for 0.5h. Unmarked peaks in Fig.2a and Fig.2b belong to WC and W_2C, respectively.

Fig. 3 The composition of (a) Al_2O_3-WC (b) CaO-WC and (c) MgO-WC pellets before and after heat treatment measured by XRF.

Fig. 4 Molar content of the equilibrium products calculated by the reactions between 5mol WC and 1mol M_xO_y as a function of the temperature at a vacuum level of 5Pa. (a) MgO-WC, (b) CaO-WC and (c) Al_2O_3-WC. The calculations on M_xO_y only

without WC additions are shown in 4d-4f for a comparison.

Figure captions in the Supplementary

Fig.S1 The electron diffraction pattern (a) and EDS spectrum (b) of impurity phases in the commercial ZrB_2 powder purchased from H.C. Starck (marked in 1i and 1j).

Fig.S2 The XRD pattern of raw Al_2O_3 powder, all the peaks could be indexed to γ type.

Fig.S3 Equilibrium products predicted in 5mol WC-1mol Y_2O_3 and 5mol WC-1mol Fe_2O_3. The calculation parameters are the same as that in Fig.4.

Fig.S4 Equilibrium products predicted in 5mol B_4C-1mol CaO. The calculation parameters are the same as used in Fig.4. The change of some gaseous substance, e.g. $BO_x(g)$, was not plotted in this figure for simplicity.

Table(I)

Table I Typical oxide impurities observed in ZrB_2 based ceramics from different research groups, including their processing details and the corresponding flexural strength at room temperature (RT) and 1600°C.

Research Group	ZrB_2 Starting Powder	Composition	Sintering parameters	Oxide morphology	Composition of the impurity	3pt-flexural strength /MPa	
						RT	1600°C
SIC-CAS [5]	Self-made ZrO_2+B_4C	ZrB_2-20vol%SiC	Hot-pressing 1900°C	Facet	Ca-Al-Si-Mg-Y-C-O and *h*BN	546±55	460±31
SIC-CAS [6]	Self-made ZrO_2+B_4C+C	ZrB_2-20vol%SiC	Hot-pressing 1900°C	Facet	Zr-Al-Si-Y-Ca-O and *h*BN	671±19	471±32
Missouri S &T [19]	Grade B ZrB_2, H.C. Starck	ZrB_2-10vol%ZrC	Hot-pressing 1900°C	Spherical	ZrO_2 and Zr-Al-Si-Ca-O	596 ± 111*	378 ± 32*
University of Arizona [22]	Grade B ZrB_2, H.C. Starck	ZrB_2+0.25wt%B_4C	Spark Plasma Sintering (SPS) at 1900°C	Spherical and facet	Ca-O-N-C, Ca-Fe-Y-Al-Ag-O and Fe-Co-O	660 ± 68	N/A
Missouri S &T [23]	Grade B ZrB_2, H.C. Starck	ZrB_2-20vol%SiC-5vol%B_4C	Hot-pressing 1900°C	Wet by the GB	Ca, Y, Al, Fe, Ni, and U, O	695 ± 69*	569 ± 56*
SIC-CAS [11,13]	Self-made ZrO_2+B_4C	ZrB_2-20vol%SiC-5vol%WC	Hot-pressing 1900°C	Not found	Not found	546±21	675±33

*Values were measured by four-point flexural test.

Figure(1)

Click here to download high resolution image

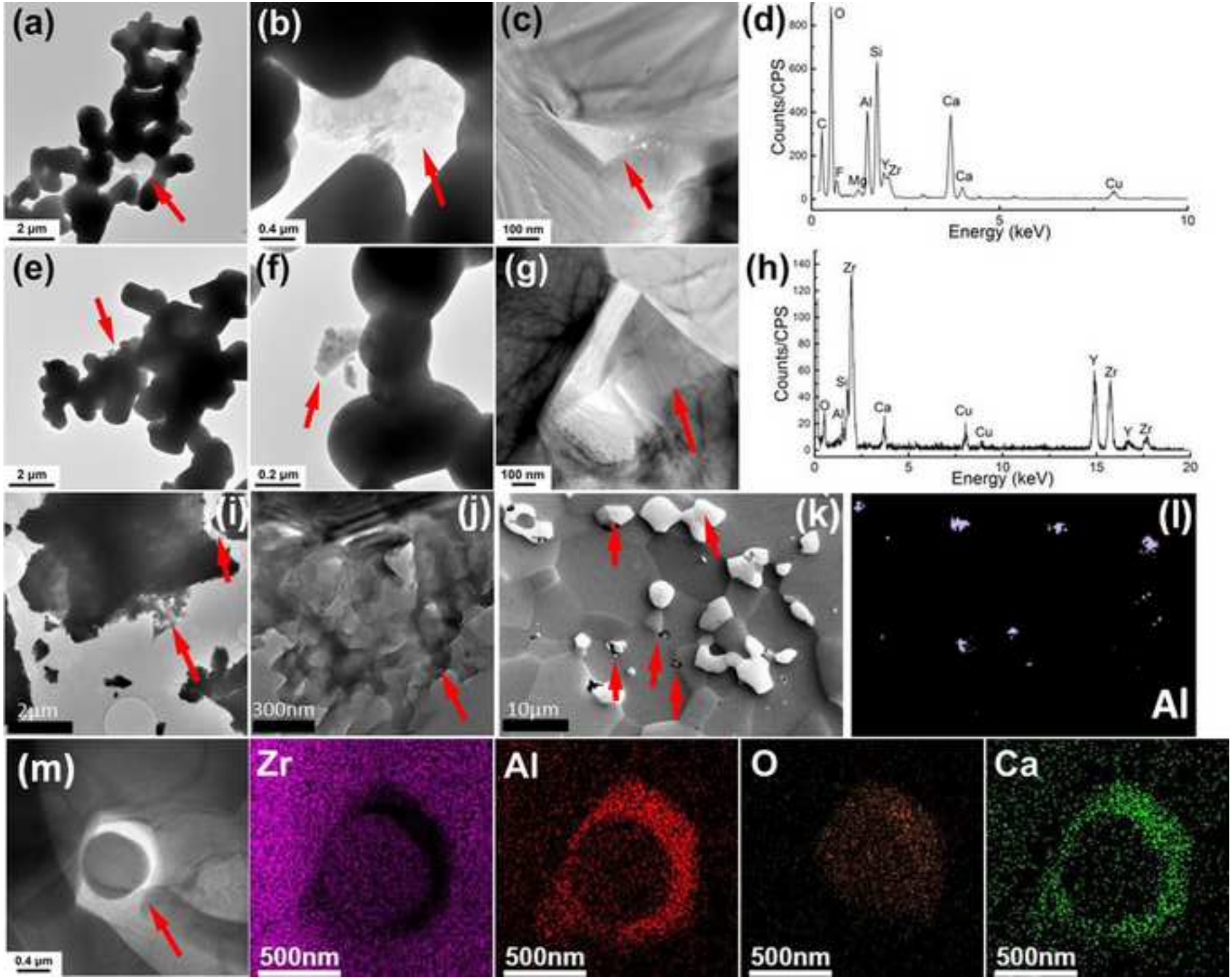

Figure(2)
Click here to download high resolution image

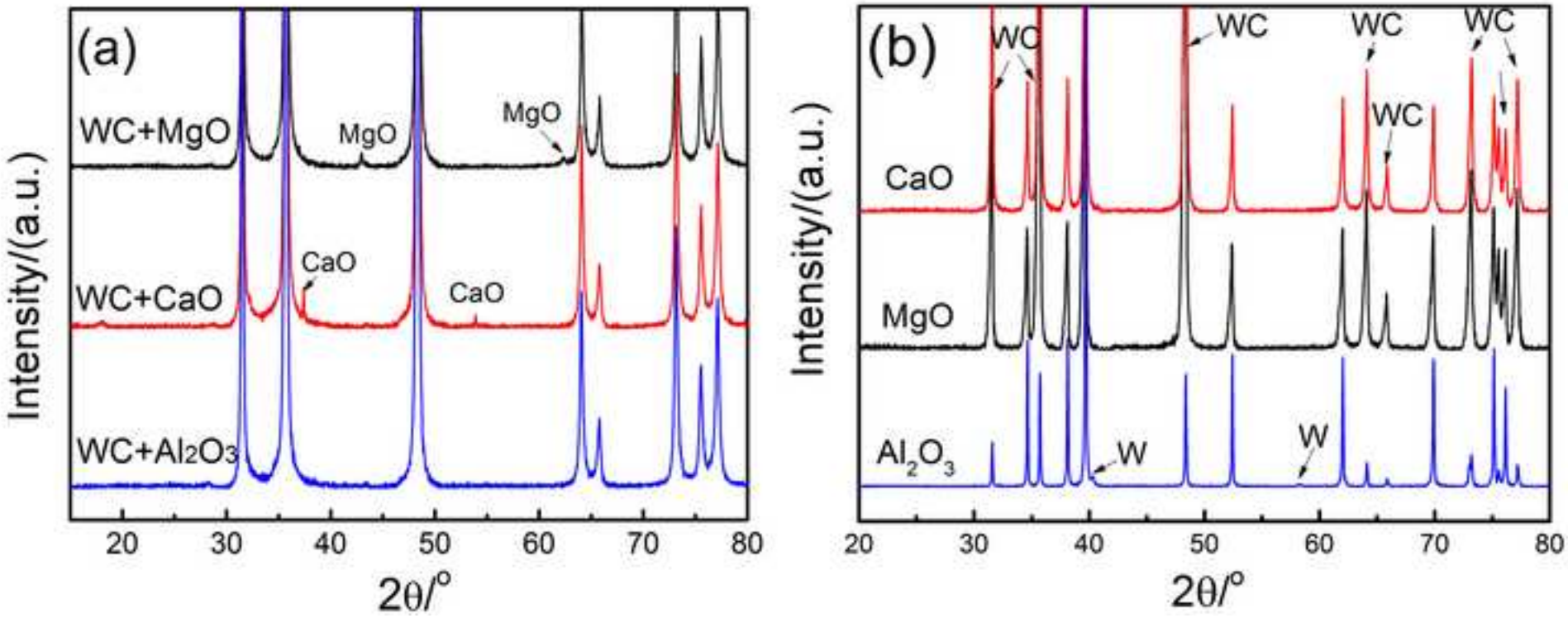

Figure(3)
Click here to download high resolution image

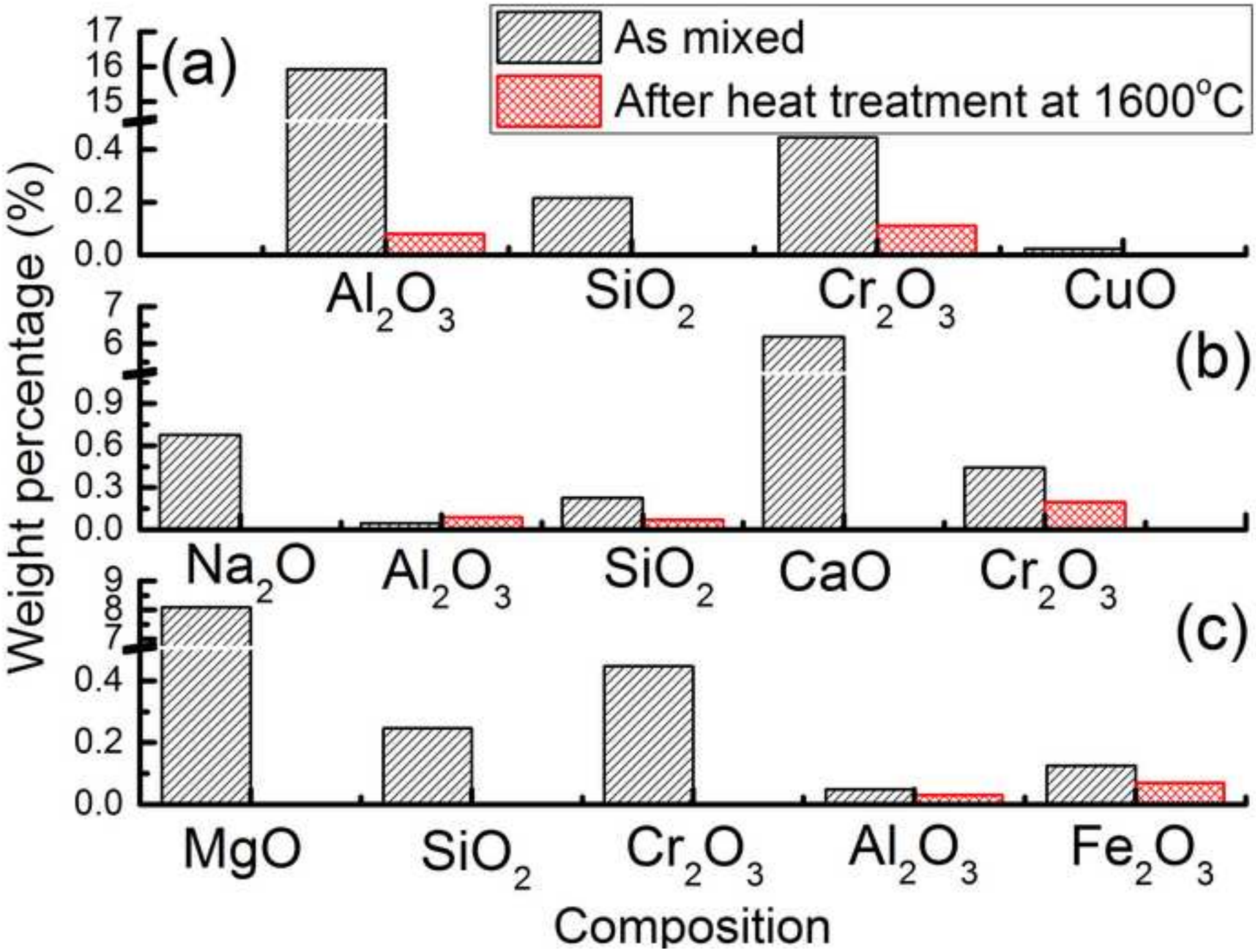

Figure(4)

Click here to download high resolution image

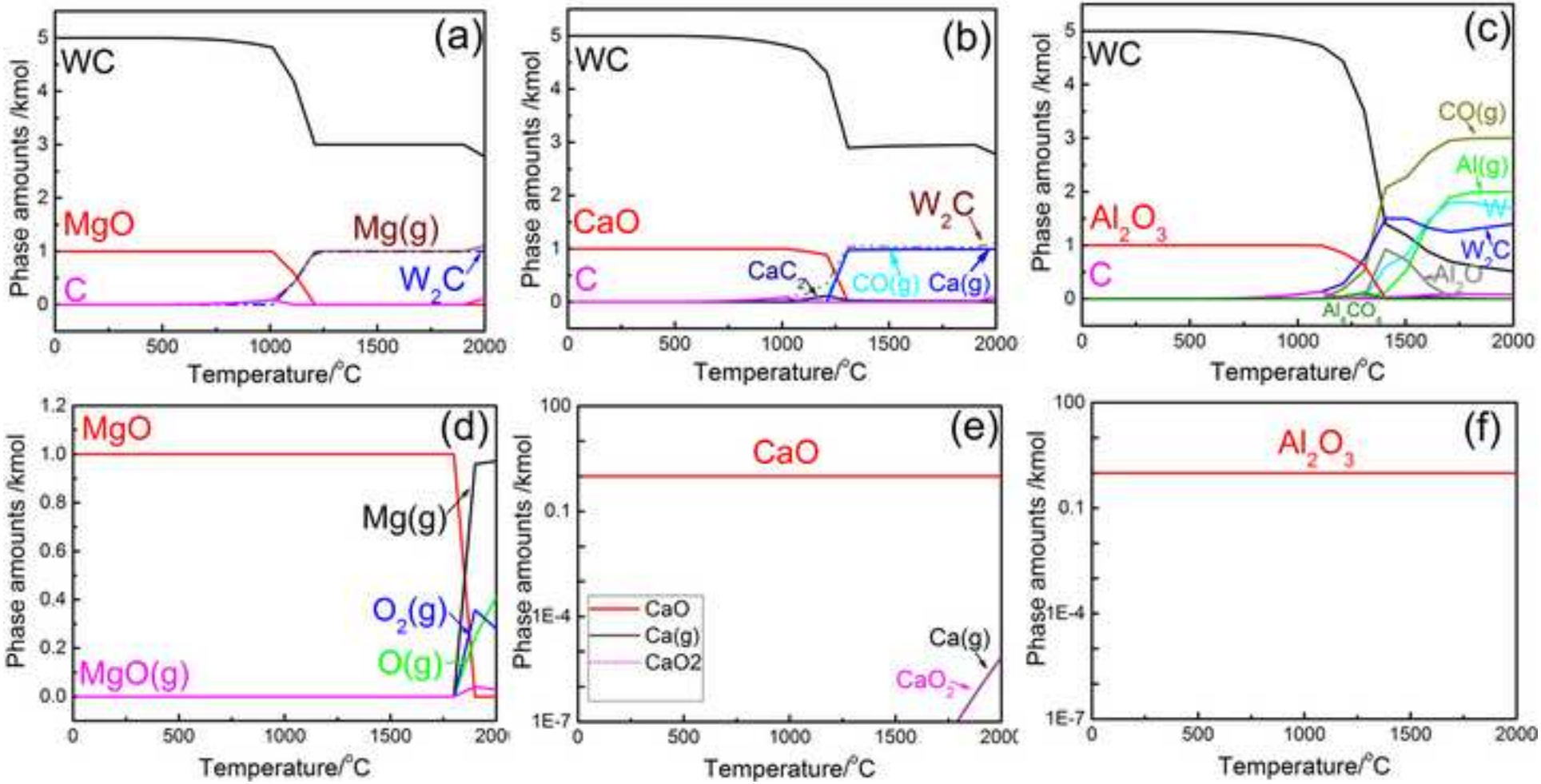

Supplementary Material Figure S1

Click here to download Supplementary Material: Figure S1.jpg